Monthly Notices
of the
ROYAL ASTRONOMICAL SOCIETY

MNRAS **462,** S491–S506 (2016)
Advance Access publication 2016 September 9

doi:10.1093/mnras/stw2413

Evolution of water production of 67P/Churyumov–Gerasimenko: an empirical model and a multi-instrument study

Kenneth C. Hansen,[1⋆] K. Altwegg,[2] J.-J. Berthelier,[3] A. Bieler,[1] N. Biver,[3] D. Bockelée-Morvan,[3] U. Calmonte,[2] F. Capaccioni,[4] M. R. Combi,[1] J. De Keyser,[5] B. Fiethe,[6] N. Fougere,[1] S. A. Fuselier,[7,8] S. Gasc,[2] T. I. Gombosi,[1] Z. Huang,[1] L. Le Roy,[2] S. Lee,[9] H. Nilsson,[10] M. Rubin,[2] Y. Shou,[1] C. Snodgrass,[11] V. Tenishev,[1] G. Toth,[1] C.-Y. Tzou,[2] C. Simon Wedlund[12,13] and the ROSINA team

[1]*Department of Climate and Space Sciences and Engineering, University of Michigan, Ann Arbor, MI 48109, USA*
[2]*Space Research and Planetary Sciences, University of Bern, CH-3012 Bern, Switzerland*
[3]*LESIA, Observatoire de Paris, LESIA/CNRS, UPMC, Université Paris-Diderot, F-92195 Meudon, France*
[4]*INAF-IAPS, Istituto di Astrofisica e Planetologia Spaziali, via del fosso del Cavaliere 100, I-00133 Rome, Italy*
[5]*Royal Belgian Institute for Space Aeronomy (BIRA-IASB), B-1180 Brussels, Belgium*
[6]*Institute of Computer and Network Engineering, TU Braunschweig, D-38106 Braunschweig, Germany*
[7]*Department of Space Science, Space Science and Engineering Division, Southwest Research Institute, San Antonio, TX 78238, USA*
[8]*University of Texas at San Antonio, San Antonio, TX 78249, USA*
[9]*Jet Propulsion Laboratory, Pasadena, CA 91109, USA*
[10]*Institutet för Rymdfysik (IRF), Box 812, SE-981 Kiruna, Sweden*
[11]*Department of Physical Sciences, Planetary and Space Sciences, The Open University, Milton Keynes, MK7 6AA, UK*
[12]*Department of Physics, University of Oslo, PO Box 1048 Blindern, N-0316 Oslo, Norway*
[13]*Department of Radio Science and Engineering, Aalto University, School of Electrical Engineering, PO Box 13000, FI-00076 Aalto, Finland*

Accepted 2016 September 20. Received 2016 September 15; in original form 2016 July 6

ABSTRACT

We examine the evolution of the water production of comet 67P/Churyumov–Gerasimenko during the Rosetta mission (2014 June–2016 May) based on *in situ* and remote sensing measurements made by Rosetta instruments, Earth-based telescopes and through the development of an empirical coma model. The derivation of the empirical model is described and the model is then applied to detrend spacecraft position effects from the Rosetta Orbiter Spectrometer for Ion and Neutral Analysis (ROSINA) data. The inter-comparison of the instrument data sets shows a high level of consistency and provides insights into the water and dust production. We examine different phases of the orbit, including the early mission (beyond 3.5 au) where the ROSINA water production does not show the expected increase with decreasing heliocentric distance. A second important phase is the period around the inbound equinox, where the peak water production makes a dramatic transition from northern to southern latitudes. During this transition, the water distribution is complex, but is driven by rotation and active areas in the north and south. Finally, we consider the perihelion period, where there may be evidence of time dependence in the water production rate. The peak water production, as measured by ROSINA, occurs 18–22 d after perihelion at $3.5 \pm 0.5 \times 10^{28}$ water molecules s^{-1}. We show that the water production is highly correlated with ground-based dust measurements, possibly indicating that several dust parameters are constant during the observed period. Using estimates of the dust/gas ratio, we use our measured water production rate to calculate a uniform surface loss of 2–4 m during the current perihelion passage.

Key words: methods: miscellaneous – comets: general – comets: individual: 67P/CG.

⋆ E-mail: kenhan@umich.edu

1 INTRODUCTION

Comets have provided wonder and fascination since first observed in the sky. Early civilizations realized that bright comets unexpectedly emerge from the darkness of the night sky and rapidly become brighter and occupy an increasing part of the sky. Eventually, these objects fade away in a few months and disappear into the celestial background. After the emergence of astronomical spectroscopy, it became evident that these bright comets were mainly composed of well-known gases and carbon- and silicon-dominated dust. Comets are believed to be the least processed bodies remaining from the early stages of the formation of our Solar system, so gaining knowledge of their chemical, mineralogical, elemental and isotopic composition is important to improve our understanding of our own origins.

Our modern understanding of comets can be traced back to Whipple (1950) who introduced the hypothesis that comets are associated with solid ice-rock conglomerates that heat up as they approach the sun and release volatile gases from their surface layers. Ground-based observations supported this hypothesis and the first close comet flybys by the Vega (Sagdeev et al. 1986) and Giotto (Keller et al. 1986) spacecraft fully validated it.

The long-term evolution of the production of water and other volatiles in comets should inform our understanding of the composition and structure of the nucleus and the processes that lead to sublimation. Unfortunately, there are several issues that make long-term monitoring of a comet during its passage through the Solar system difficult. Due to simply the availability of observing platforms, the vast majority of measurements of the cometary dust and gas coma have been made by ground-based telescopes (Bockelée-Morvan et al. 2004). Many ground-based telescopes that can observe brighter comets exist and because the access to these medium-size telescopes is reasonable, many comets have been monitored during the near-sun phases of their Solar system passage. The major issue with ground-based measurements is that they are limited due to the transmission windows of the atmosphere. Although water is the most abundant volatile produced at comets, the vast majority of cometary measurements made from the ground are of the dust coma or of highly visible optical transitions. Typical species measured include HCN, C_2 and C_3 (Schleicher 2006; Lara et al. 2011). While in some cases, these species may serve as proxies for the production of water or other more volatile species and may even themselves provide important clues to the understanding of cometary evolution, they are minor species that do not necessarily track the water production or lead to a deeper understanding of the water production during a comet's perihelion passage.

Direct ground-based infrared measurements of water in comets are quite good at yielding water production rates for moderate to bright comets at moderate to small heliocentric distances (see Bockelée-Morvan et al. 2004). Water has also been directly measured at longer microwave wavelengths from various space-based platforms (e.g. Lecacheux et al. 2003; Bensch et al. 2004; Hartogh et al. 2010; Hartogh et al. 2011; Ootsubo et al. 2012). Otherwise, water production rates are most often inferred from either ground-based (e.g. Schleicher 2006) or space-based observations of OH (e.g. Weaver et al. 1981) or from space-based observations of atomic H (Combi et al. 2005). Still, none of these types of observations can yield water production rates from a Jupiter family comet like 67P/CG covering the full range of heliocentric distance out to >3.5 au.

Due to the limitation of both ground-based and space-based measurements, long-term monitoring of the water production rate extending to large heliocentric distances does not exist for most comets. The prominent exception to this are the brightest comets such as comet C/1995 O1 Hale-Bopp (Kührt 1999; Biver et al. 2002) and 1P/Halley (Gehrz et al. 2005). However, Hale-Bopp and Halley are atypical comets due to their very high production rates, therefore their high apparent brightness and easy observability.

The current passage of 67P/CG through the inner Solar system is the fourth that has been observed. During each of the previous three passages, the dust brightness was measured as well as the production of the easily observable minor radical species (Schulz, Stüwe & Boehnhardt 2004; Weiler, Rauer & Helbert 2004). In addition, the water production was determined near perihelion during the previous three passages through SWAN/SOHO Lyman α observations (Bertaux et al. 2014). Interest in observing 67P/CG greatly increased due to the selection of 67P/CG as the target of the Rosetta mission (Schleicher 2006; Lara et al. 2011; Tubiana et al. 2011; Bertaux et al. 2014; Guilbert-Lepoutre et al. 2014). The current passage of 67P/CG presents a unique opportunity to measure the evolution of the water production rate in high resolution as a function of heliocentric distance via both Earth-based telescopes and *in situ* Rosetta measurements.

The water production rate as a function of heliocentric distance provides an important constraint on the rate and method of water sublimation from the comet and hence important information about the sub-surface. Keller et al. (2015) examined the effect of varying degrees of insulation on the production rate of water using a two layer model – a thin, porous dust layer above an icy surface. They find that a dirty ice surface with a thin dust cover of 50 μm yields production rates similar to rates measured during previous apparitions of 67P/CG at perihelion. The model predicts water production to a heliocentric distance of 5 au, however, the work compares only to the previous apparition and water production rates within about ± 100 d ($\sim$1.75 au) of perihelion.

This paper investigates the evolution of the gas production by comet 67P/CG during the 2014 June–2016 April period when its heliocentric distance varied from $\sim$4.0 au pre-perihelion through perihelion at 1.24 au to $\sim$2.7 au post-perihelion.

2 DERIVATION OF AN EMPIRICAL COMA MODEL

Comet 67P/CG's water coma exhibits a complex, non-uniform distribution that varies in time due to both the rotation of the comet as well as the orbital motion of the comet. While Rosetta presents a large step forward in sampling that distribution, it cannot measure the water distribution at all locations at all times. For this reason, the interpretation of Rosetta measurements requires the use of models. These models can be as simple as assuming a spherically symmetric, uniformly expanding coma (Haser 1957) or as sophisticated as Direct Simulation Monte Carlo (DSMC) models of the 3D neutral gas coma using an accurate shape model (Bieler et al. 2015; Fougere et al. 2016a,b). The value of a simple, analytic model such as Haser (1957) is both its ease of application as well as the ease with which intuition can be applied to its use. However, with a shape as complex as that of the nucleus of 67P/CG, it is clear that a simple spherical model is not sufficient. The DSMC models of Bieler et al. (2015) and Fougere et al. (2016a,b) are a major step forward because they model the water production of 67P/CG using an accurate shape model, accurately calculated solar illumination (including shadowing) and physically meaningful modelling techniques. These models are developed and calibrated using ROSINA (Rosetta Orbiter Spectrometer for Ion and Neutral Analysis) data

and have then been shown to accurately reproduce the measurements of both ROSINA and the VIRTIS (Visible InfraRed Thermal Imaging Spectrometer instruments). While these models are extremely useful, their outputs are difficult to interpret both due to complexities associated with the shape, as well as the difficulty of dealing with the data structures and the shear volume of their numerical output. It is clear that the analytic, spherically symmetric model (Haser 1957) and the sophisticated numerical models (Bieler et al. 2015; Fougere et al. 2016b,a) are at either end of a spectrum of models used for analysis of this type of observational data.

One purpose of this work is to develop an empirical model of the water coma of 67P/CG derived from the DSMC numerical models of Fougere et al. (2016b). Clearly, the model cannot retain all the information contained in the full 3D numerical results, but a closed form, analytic model that represents some of the more important features of the complex DSMC results could greatly benefit the community working to interpret the Rosetta measurements.

2.1 The DSMC model

All DSMC model results presented here are derived directly from the model runs of Fougere et al. (2016b) that used the Adaptive Mesh Particle Simulator code (Tenishev, Combi & Davidsson 2008; Tenishev, Combi & Rubin 2011). Fougere et al. (2016b) describe the process used to develop, verify and apply their model to 67P/CG. The most important aspects of their method are described here for clarity. Fougere et al. (2016b) use ROSINA data to produce a spherical harmonic map of the activity of the surface. This activity map represents the relative response of the surface to solar illumination. Using the activity map, the authors perform DSMC simulations for four different heliocentric distances (3.5, 2.7, 2.2 and 1.7 au). At each distance, they perform 12 simulations, spaced one hour apart, that together model a single rotation of comet 67P/CG. Comparing results from these 48 cases to both ROSINA and VIRTIS measurements, Fougere et al. (2016b) find that their DSMC models, using a single activity map, combined with accurately calculated solar illumination, do a very good job of reproducing Rosetta measurements. Since the publication of Fougere et al. (2016b), the authors have performed additional simulations at 1.5 au inbound, 1.24 au (perihelion) and outbound at 1.5 au that we will also use in this work. In a new paper, Fougere et al. (2016a) re-examine their activity map, extend their work to the outbound equinox and include new species (CO_2, CO and O_2). This new work did not drastically modify the water results published in Fougere et al. (2016b) on which this work is based.

2.2 The empirical model

To derive an empirical model, we extract spherical 'slices' from the DSMC model of Fougere et al. (2016b) for each of the seven heliocentric distances (inbound: 3.5, 2.7, 2.2, 1.7, 1.5, 1.24 au; outbound 1.5 au) for each of the 12 rotation phases. We extract the water density on spheres of 10, 32 and 100 km so that the densities will be very close to factors of 10 different due to the $1/r^2$ expansion factor.

DSMC model results are in a comet-fixed (cf) coordinate system that rotates with the comet. For our empirical model, we prefer a Sun-fixed (sf) coordinate system where the x-axis points from the comet to the Sun, the z-axis is chosen so that the x–z plane contains 67P/CG's rotation axis with the positive axis being towards the north, and where the y-axis completes the system. Each of the 252 extracted slices is rotated to this sf coordinate system. Throughout the rest of this work, cf- and sf- will be used to indicate the two different coordinate systems (i.e. sf-longitude indicates longitude in the Sun-fixed frame).

Including the full rotational information in the empirical model would introduce the same complexities as the full DSMC model. For this reason, we average the slices extracted from the DSMC model over the 12 simulation runs that represent a single rotation. Fig. 1 shows the average water distribution for each of the seen heliocentric distances we used to derive our empirical model. An important feature of the DSMC averages is symmetry in sf-longitude at all heliocentric distances. On the other hand, the peak of the water distribution is not at the sub-solar point for any of the heliocentric distances, but is shifted in sf-latitude. Additionally, the rotation averages indicate that the distribution does not have the same spread in sf-longitude as sf-latitude. These are important features to retain as we develop the empirical model.

The distribution that best fits our DSMC model rotationally averaged densities is

$$n = \frac{f\,Q}{4\pi r^2 v}, \tag{1}$$

where n is the density, Q is the production rate, r is the radial distance from the comet and v is the gas velocity. Factor f introduces the sf-latitude and sf-longitude dependence of the distribution. For $f = 1$, the model is just a spherically symmetric radial expansion. The factor f is a stretched, offset Gaussian given by

$$f = ae^{-\psi^2/\lambda'^2} + b. \tag{2}$$

In this equation, ψ is a modified phase angle and λ' is the width of the distribution (both in degrees) and a and b are dimensionless parameters. The DSMC model rotation averages indicate that the peak of the neutral distribution is in the x–z plane but offset above or below the x–y plane. Because the DSMC distribution is roughly uniformly distributed around the peak, the model should depend on the angular distance away from the peak. Such an angle would typically be referred to as a phase angle, if measured from the Sun-comet line. We compute ψ, our offset phase angle, using the following approximate formula

$$\cos\psi = \sin\theta_{\rm of}\sin\theta + \cos\theta_{\rm of}\cos\theta\cos\phi, \tag{3}$$

where θ and ϕ are sf-latitude and sf-longitude and $\theta_{\rm of}$ is the offset of the peak in sf-latitude. The width of the distribution is given by

$$\lambda' = \lambda/\theta_{\rm s}, \tag{4}$$

where λ is a parameter and $\theta_{\rm s}$ is a stretching factor that stretches the distribution in sf-longitude given by

$$\theta_{\rm s} = 1 + c_1\,(\theta - \theta_{\rm of})\,, \tag{5}$$

with c_1 controlling the amount of stretching. Angles in equations (4) and (5) are in degrees.

In equations (1)–(5), the parameters $\theta_{\rm of}$, c_1, λ, a, b and v must be determined. All parameters other than velocity, v, are determined by computing the least-squares fit of the equations to the rotationally averaged DSMC slices at each heliocentric distance and cometocentric distance. Fig. 1 shows the result of the fitting in the middle column. A visual comparison of the left-hand (DSMC average) and the middle (fit) columns shows that the fits are quite good. Quantitatively, we compute the root mean square (rms) difference between the fit and the DSMC average and find that for each of the cases, rms difference is than 0.5 per cent. For each of the parameters for all cases, the formal statistical uncertainty is less than 0.1 per cent. We performed a second sensitivity study by varying one parameter

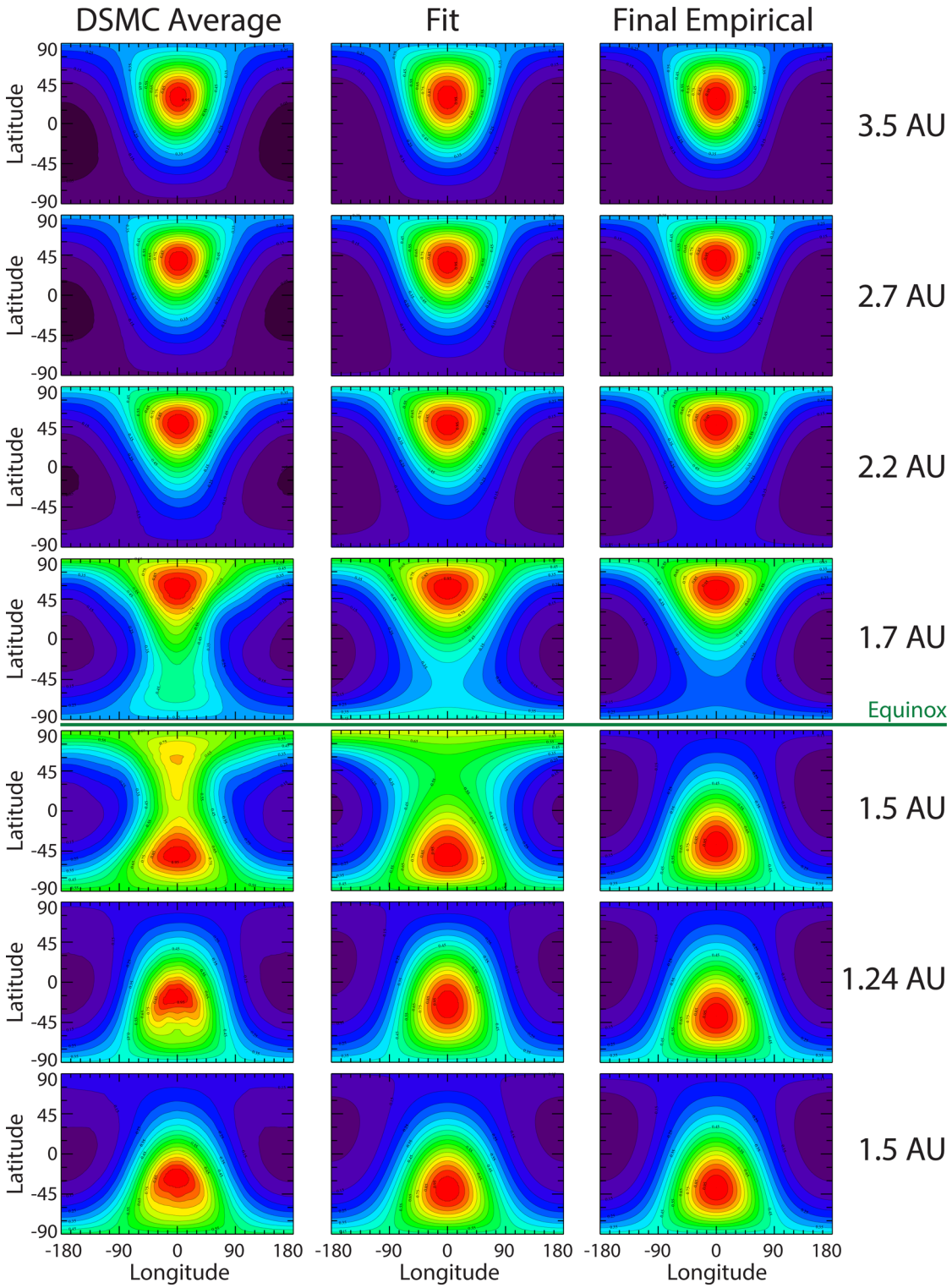

Figure 1. Water distribution in the sf-frame for the rotationally averaged DSMC slices (left-hand column), the best fit of equations (1)–(5) to the DSMC averages (centre column) and the final empirical model (right-hand column). In each panel, the distribution is scaled to the peak density with contour intervals that are 5 per cent of the maximum. Each row represents a different heliocentric distance with inbound at top and outbound at bottom. In each frame, sf-longitude is along the x-axis (-180° to 180°), with sf-latitude along the y-axis (-90° to 90°). All figures are for a cometocentric distance of 32 km.

of the fit by 10 per cent while holding all others constant. This test resulted in increase in the rms difference of up to a factor of 4, but still resulted in RMS differences not larger than a few per cent. The closeness of the fits in reproducing the DSMC averages shows that the empirical model is well suited to describing the rotationally averaged DSMC results. The velocity is selected so that the least-squares fit has a total production rate that is the same as the total production rate of the DSMC model average for each case.

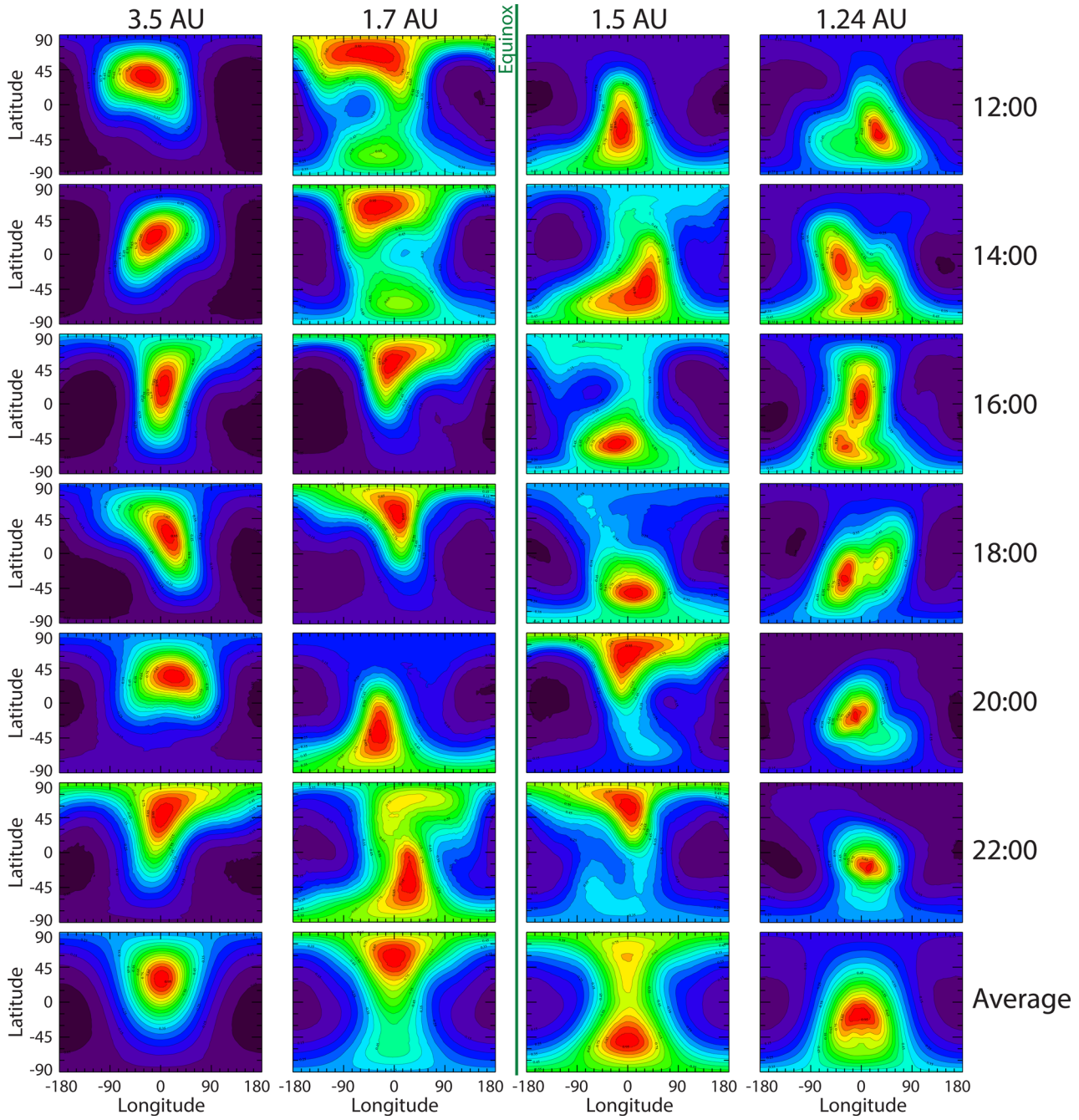

Figure 2. Water distribution for individual rotations phases for a subset of heliocentric distances and rotation phases. In each panel, the distribution is scaled to the peak density with contour intervals that are 5 per cent of the maximum. Columns represent four different interesting heliocentric distances, while rows represent the different rotation phases. The DSMC model of Fougere et al. (2016b) provides 12 different rotation simulations at each heliocentric distance separated by one hour each and representing an entire rotation of 67P/CG. The simulations are performed for a specific date, with the first simulation in each set starting at noon. Therefore, rows in this figure do not represent times when the comet had the same cf-longitude pointing to the Sun and should not be compared directly to each other. Here we show every other rotation simulation and the average for comparison. In each frame, sf-longitude is along the x-axis (-180° to 180°), with sf-latitude along the y-axis (-90° to 90°). All figures are for a cometocentric distance of 32 km.

While it is clear in Fig. 1 that the least-squares fit to the DSMC average is good, we also compare the individual rotation phases to the DSMC average. Figs 2 and 3 give an indication of how rotation of the nucleus affects water distribution. In Fig. 2, the rotation of the nucleus is seen by following frames down a column. The 3.5 au case is a simple example. This case shows that each different rotation orientation produces a distribution that is not symmetric in sf-longitude, but, when averaged, produces a symmetric distribution. The cases near equinox (1.5 and 1.7 au) show very high variability due to rotation and at times show peaks in both the north and the south simultaneously. However, when averaged, these cases still produce only one main peak in either the north or the south and are still sf-longitudinally symmetric (this will be discussed in more detail below). Fig. 3 shows the water density extracted along the sf-latitude $=0^\circ$ and sf-longitudes $=0^\circ$ lines from each of the rotation phases shown in Fig. 2. The rotation phases are compared

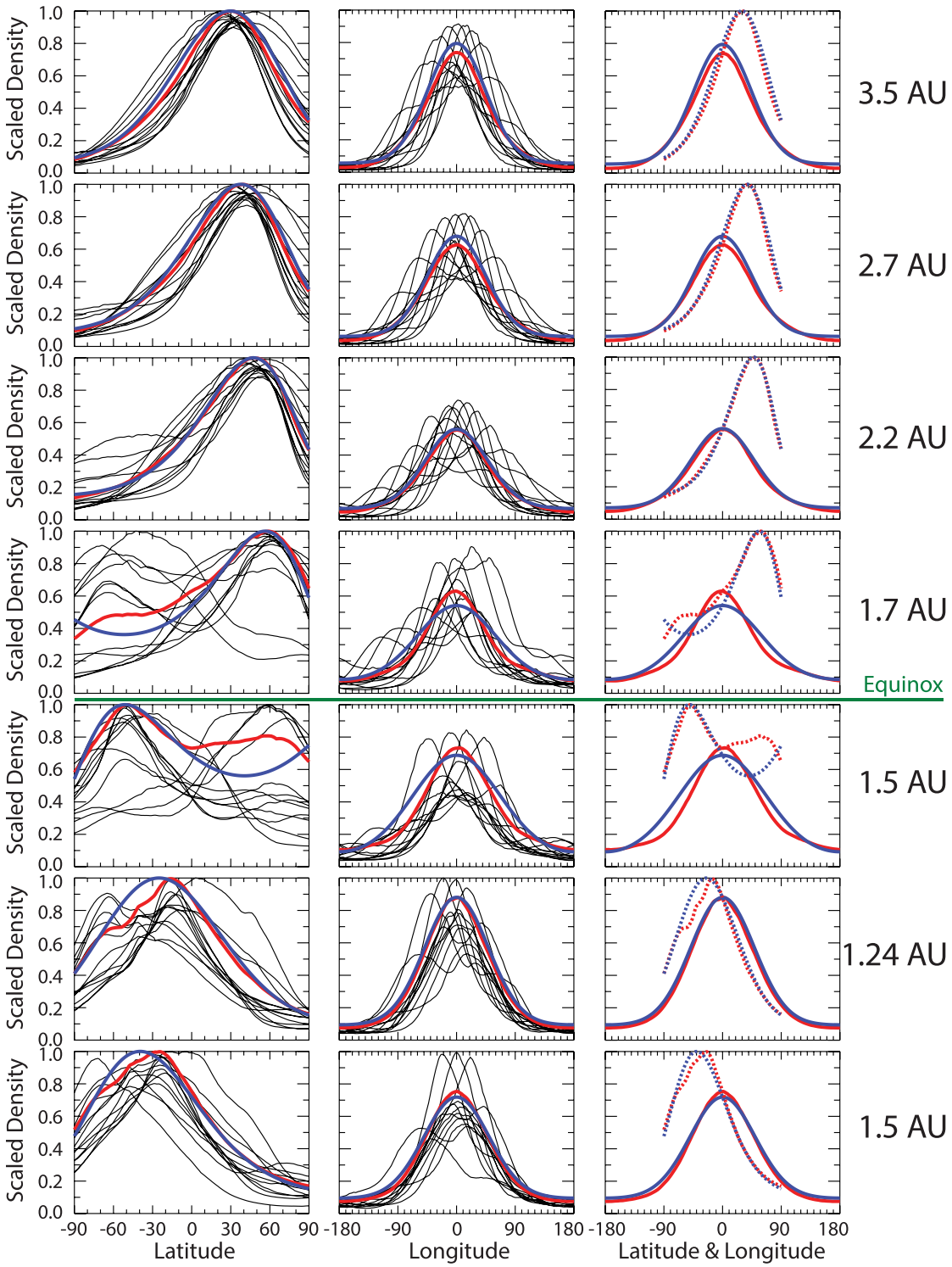

Figure 3. Water distribution for each DSMC rotation phase compared to the DSMC average and the least-squares fit. For each heliocentric distance, the distribution is scaled to the peak density. In each panel, black: individual DSMC rotation phases, red: DSMC rotationally averaged, blue: least-squares fit empirical model. Left-hand column: sf-longitude=0°, centre column: sf-latitude=0°, right-hand column: comparison of DSMC average versus fit for both the sf-latitude (dotted lines) and sf-longitude (solid lines). Each row represents a different heliocentric distance with inbound at the top and outbound at the bottom. In each frame, angle is along the *x*-axis. Values on the *y*-axis is normalized to the peak of the water distribution.

to both the DSMC average and the least-squares fit. In the figure, variation due to the rotation is even more evident than in Fig. 2. The rows for 1.5 and 1.7 au clearly show the double peak in some of the rotation cases in contrast to heliocentric distances before equinox (that occurred at 1.67 au inbound) and both during and after perihelion where distributions mostly have a single peak in sf-latitude and have less scatter. Figs 2 and 3 show that there are significant density variations that are averaged out in the empirical model. However,

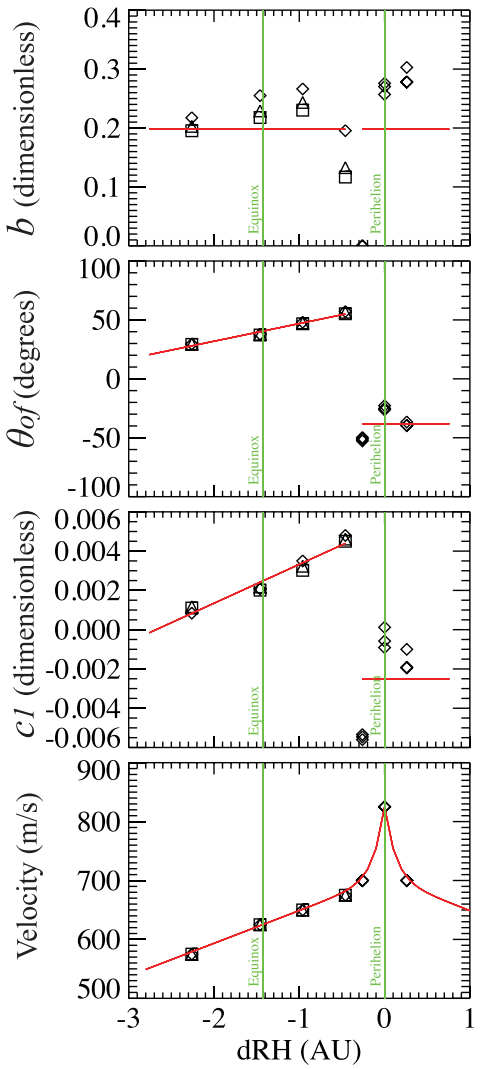

Figure 4. Empirical model parameters that are a function of heliocentric distance only plotted against the distance from perihelion (dRH). In each frame, discrete parameters determined by fitting the empirical model to the DSMC average are shown as diamonds (10 km cometocentric distance), triangles (32 km) and squares (100 km). For all plotted parameter values, the formal statistical uncertainty is less than 0.1 per cent (less than the size of the point). The red curve is a piece-wise linear fit to the data as function of heliocentric distance. Parameters of the red curves are given in Table 1. Top panel: b, second panel: $\theta_{\rm of}$, third panel: c_1, bottom panel: v. Note that velocity requires a special treatment (see equation 7).

the averages are fairly representative of the individual rotation cases and the empirical model fits the rotation-averaged distributions very well.

As noted above, we first fit the empirical model to the individual, rotationally averaged DSMC results at discrete heliocentric and cometocentric distances. The process results in parameters for the empirical model that are valid at only these discrete points. In order for the empirical model to be a continuous function of heliocentric and cometocentric distances, we next generalize the empirical model parameters by fitting a piece-wise linear function to the discrete values of each parameter as a function of either heliocentric or cometocentric distance. Fig. 4 shows the parameters that we find are a function of heliocentric distance only ($\theta_{\rm of}$, c_1, b and v). In these figures, the parameter values from fits at discrete cometocentric distances show very little scatter and therefore need to be parametrized as a function of heliocentric distance only. We find that all parameters show a drastic change in value across the inbound equinox at 1.67 au. Therefore, we parametrize the heliocentric distance dependence using piece-wise linear functions – one function before inbound equinox, and one after the inbound equinox through perihelion. Furthermore, for all parameters, there is no clear trend for the values after the inbound equinox (1.5 au inbound and 1.5 and 1.24 au outbound), therefore we use constants for the parameters. Values for the piece-wise linear fits of the parameters as a function of heliocentric distance are given in Table 1. Values in the table can be used to calculate the parameters that depend on heliocentric distance only using

Table 1. Parameter values for the empirical model, equations (6) and (8).

Parameter	Unit	$r_{\rm h}$ dependence $m_{r_{\rm h}}$	$r_{\rm h}$ dependence $b_{r_{\rm h}}$	r dependence $m_{\rm r}$	r dependence $b_{\rm r}$	Scalefactor ($f_{\rm r}$)
Before inbound equinox (>1.67 au)						
$\theta_{\rm of}$	deg	−15	80.5	–	–	–
c_1	–	−0.001 98	0.007 76	–	–	–
λ	deg	3.99	42.5	0.0816	52.5	56.3624
a	–	–	3.60	−0.007 24	3.55	3.207 31
b	–	–	0.198	–	–	–
v	m s^{-1}	−55.5	771.0	–	–	–
Between equinoxes, including perihelion						
$\theta_{\rm of}$	deg	–	−38.2	–	-	–
c_1	–	–	−0.002 51	–	–	–
λ	deg	–	61.4	–	–	–
a	–	–	2.74	–	–	–
b	–	–	0.198	–	–	–
v	m s^{-1}	−55.5	771.0	–	–	–

$$p(r_{\rm h}) = m_{r_{\rm h}} r_{\rm h} + b_{\rm h}, \tag{6}$$

where $p(r_{\rm h})$ is the value of the parameter to be used in equations (1)–(5), $m_{r_{\rm h}}$ and $b_{r_{\rm h}}$ are the slope and intercept from Table 1 and $r_{\rm h}$ is the heliocentric distance in astronomical units.

The water velocity in the bottom panel of Fig. 4 shows a dramatic increase near perihelion but is clearly linear between 3.5 and 1.7 au inbound. For this reason, we use

$$v = \left(m_{r_{\rm h}} r_{\rm h} + b_{r_{\rm h}}\right)\left(1 + 0.171 e^{-(r_{\rm h}-1.24)/0.13}\right), \tag{7}$$

where $m_{r_{\rm h}}$ and $b_{r_{\rm h}}$ are the linear fit parameters given in Table 1.

The other parameters in equations (1)–(5), λ and a, are function of both the heliocentric distance and the cometocentric distance. Fig. 5 shows the discrete fit values for these variables. Again, we find that the parameters show a systematic change in value across the inbound equinox. Other than the values for λ before the inbound equinox, we find that piece-wise constants, as a function of heliocentric distances, are the best values. Values for the piece-wise linear fits of the parameters are given in Table 1. Values in the table can be used to calculate the parameters using

$$p(r_{\rm h}, r) = (m_{r_{\rm h}} r_{\rm h} + b_{r_{\rm h}})(m_{\rm r} r + b_{\rm r})/f_{\rm r}, \tag{8}$$

where $p(r_{\rm h}, r)$ is the value of the parameter to be used in equations (1)–(5), $m_{r_{\rm h}}$ and $b_{r_{\rm h}}$ are the slope and intercept for heliocentric distance dependence from Table 1, $m_{\rm r}$ and $b_{\rm r}$ are for the cometocentric distance and r is the cometocentric distance in km.

Equations (1)–(5), the parameters in Table 1 and equation (7) (the equation for velocity) yield an empirical model of the water density for 67P/CG. The remaining parameter to determine is the

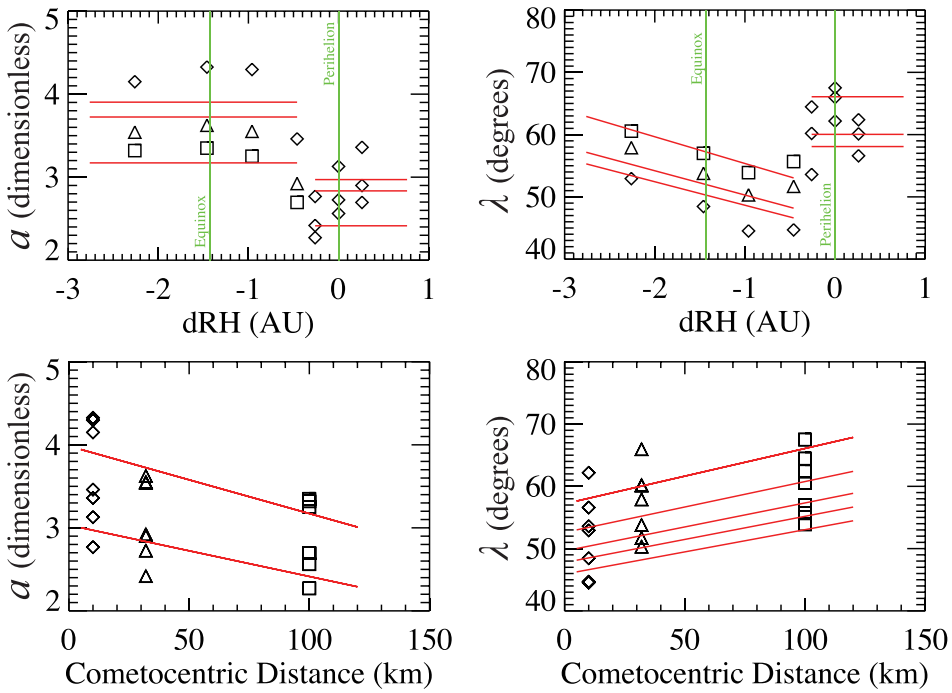

Figure 5. Empirical model parameters that are a function of heliocentric and cometocentric distance. In each frame, discrete parameters determined by fitting the empirical model to the DSMC average are shown as diamonds (10 km cometocentric distance), triangles (32 km) and squares (100 km). Uncertainties in the parameter values are the same as described in Fig. 4 The red curves are fits to the points. Parameters of the red curves are given in Table 1 and equation (8). Top row: heliocentric distance dependence plotted against the distance from perihelion. Bottom row: cometocentric distance dependence. Left: a, right: λ.

Table 2. Heliocentric dependence of the water production rate.

Data set	Method	Orbital phase	c_1	c_2
ROSINA	Empirical	Inbound	$(2.58 \pm 0.12) \times 10^{28}$	-5.10 ± 0.05
All Rosetta	Various	Inbound	$(2.59 \pm 2.75) \times 10^{28}$	-5.18 ± 0.06
ROSINA	Empirical	Outbound	$(1.58 \pm 0.09) \times 10^{29}$	-7.15 ± 0.08

total production rate, Q, as a function of heliocentric distance. It is possible to determine this parameter from the DSMC model results, but computing this function from the Rosetta data is a preferable method. Below, we use the empirical model to correct, or detrend, Rosetta measurements for spacecraft motion and then use the corrected water production measurements to determine a function for Q (see equation 10 and Table 2).

3 OBSERVATIONS AND ANALYSIS

3.1 ROSINA

DFMS (Double Focusing Mass Spectrometer) is one of the two mass spectrometers of the ROSINA instrument suite (Balsiger et al. 2007). It is designed to measure isotopic ratios and relative abundances of neutrals and ions in a mass/charge range of 12 u/e–140 u/e. In this study, we focus on measurements of neutral H_2O taken from 2014 August until 2016 May. To determine absolute abundances, we calibrate the DFMS measurements together with the ROSINA COPS (COmetary Pressure Sensor) (Balsiger et al. 2007) measurements of the total number density. The number density measurements of COPS depend on the composition of the coma of 67P/CG due to different ionization efficiencies of the measured species. Using the DFMS relative abundances together with the COPS number density results in an absolute density for each species. This calibration method produces the most accurate species abundances by correcting for several DFMS instrument specific variations (detector degradation, temperature drifts, dust deposition) that affect each species equally. ROSINA water abundances determined in this way have an uncertainty of ∼10 per cent.

Each DFMS mass/charge measurement of 18 u/e represents the density of water molecules at a specific time at a single point in the coma. In order to calculate the total water production rate from the DFMS data, it is necessary to apply a model of the water distribution in the coma. The simplest such model is to assume that the coma is spherically symmetric, however, measurements by DFMS and all other Rosetta instruments show strong heterogeneities in the coma of 67P/CG (Hässig et al. 2015). In order to correct for the non-uniform coma distribution and the location of the spacecraft, we apply the empirical model derived above to determine a correction factor. Without this correction, the total production calculated from ROSINA measurements is overestimated for data taken in high-density regions of the coma (typically the day side and/or the summer hemisphere) and underestimated for data from low-density regions of the coma (typically the terminator region and/or the winter hemisphere). The distribution of H_2O is dominated by the illumination conditions on the nucleus surface (Bieler et al. 2015) and hence varies strongly over one cometary rotation period and in a more long-term way over the orbital period of 67P/CG around the Sun. We use empirical model defined in equation (2) to determine the correction factor to account for the spatial heterogeneity of the H_2O coma. The water production rate is then calculated according to

$$Q = 4\pi v r^2 n f, \tag{9}$$

where Q is the detrended total production rate, n is the ROSINA number density, v is the outflow velocity, r is the radial distance

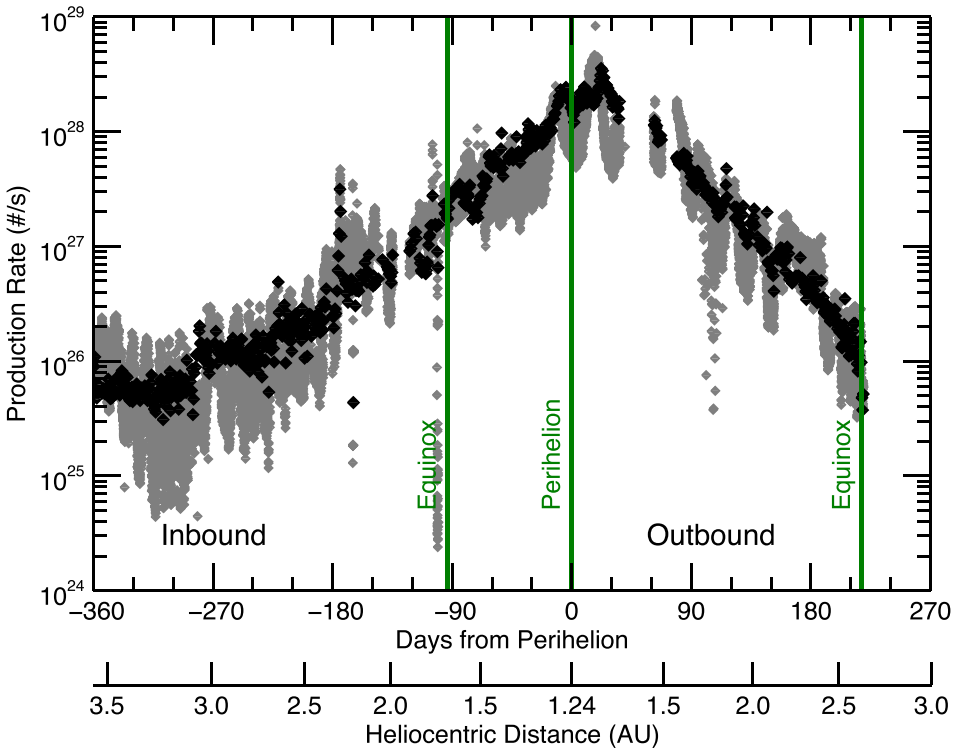

Figure 6. Water production rates computed from ROSINA number density measurements. Grey diamonds denote production rates calculated using ROSINA densities and assuming a spherically symmetric coma. This is equivalent to applying equation (9) but with $f = 1$ (no correction). Black diamonds denote production rates that are detrended for spacecraft location in the non-spherical coma using equation (9) and then averaged over a full cometary rotation.

from the comet and f is the correction factor. v and f are derived directly from the empirical model described above.

Fig. 6 shows the results of the detrending process. For comparison, the figure shows the water production rate calculated from the ROSINA data using no correction ($f = 1$) that is equivalent to assuming a spherically symmetric coma (grey diamonds). Also shown in the figure are the corrected data points. Because the empirical model used to make the correction is averaged over the rotation period of the comet, we show the empirically corrected ROSINA production rate values also averaged over a rotation period of 67P/CG (black diamonds). At this point, we note that the process of detrending and averaging the ROSINA data greatly reduces the scatter in ROSINA data (grey diamonds). A careful look at the figure, as well as Figs 7 and 8, shows that the scatter is mostly reduced due to the detrending of the spacecraft motion, but also due to the averaging. Therefore, the apparent scatter in the detrended ROSINA data (black diamonds) in Fig. 6 is very representative of the day to day variation in the rotationally averaged water production rate.

Given the many steps involved in creating the empirical model, it is difficult to determine a quantitatively precise uncertainty for each of the points in Fig. 6. As indicated above, the rms differences between the DSMC averages and the model fits is less than 0.5 per cent in all cases. However, we should also take into account the fitting demonstrated in Figs 4 and 5, the uncertainty inherent in the original ROSINA data and uncertainty in the DSMC model. As described above, ROSINA wanter abundances have an uncertainty of ∼10 per cent. Fougere et al. (2016b) note that the DSMC model and the ROSINA data have a correlation of 0.84, indicating a reasonably good match between the data and the model. The fitting in Figs 4 and 5 results in rms differences of less than 3 per cent for both the linear fits and for the special functional fit to the velocity. Where we have chosen to use constant parameter values (mostly after the inbound equinox), we have rms differences of 20–80 per cent in the parameter values. These are large differences, however, it is clear from Fig. 1 that the resulting empirical model (right-hand column) does not differ greatly from the DSMC average (left-hand column) or the fits to those averages (middle column). We have computed the rms difference between the empirical model and the fits to the DSMC average and find that the difference is less than 1 per cent in all cases. Considering the various sources of potential uncertainties, we conclude that the uncertainty of using the empirical model comes mostly from the inherent uncertainty of the ROSINA data and on the uncertainty of the original DSMC model results in matching the ROSINA data. We therefore estimate that the empirical model has an uncertainty of approximately 20 per cent.

Figs 7 and 8 show the water production rates, along with the applied empirical correction factor and several different spacecraft ephemeris quantities. Fig. 7 shows an inbound period well before equinox. During this time, the water production peaked at northern latitudes (Hässig et al. 2015). The figure shows that Rosetta was executing terminator orbits, remaining at nearly 90° phase angle for the entire 90 d period. During this time, Rosetta's orbit takes it alternately over the Northern, then Southern hemispheres of the comet, generating the observed oscillation in the non-corrected ROSINA data. In the sun-fixed coordinate system (shown in the bottom panel), the spacecraft goes directly over the coordinate system pole, resulting in the jump in longitude. The most important feature of this figure is the empirical correction factor shown in the second panel. From the plot, it is clear that when the spacecraft executes terminator orbits, using a spherically symmetric coma to estimate

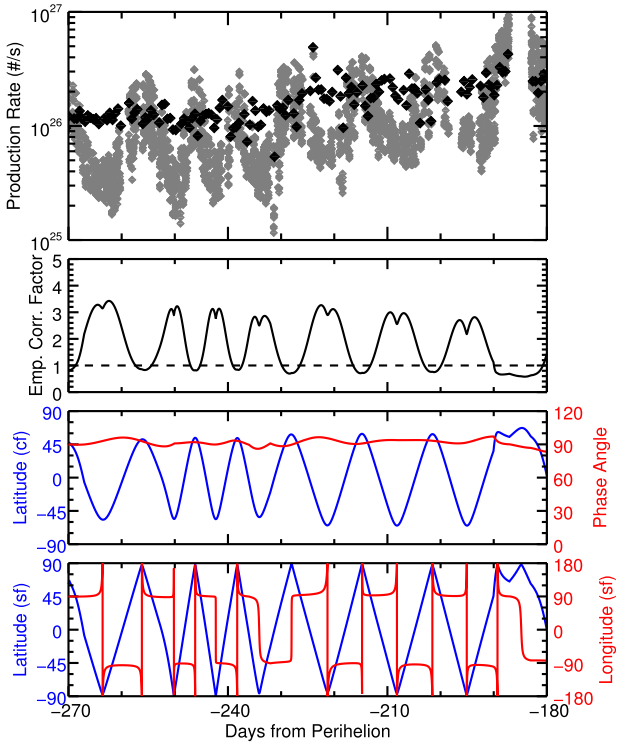

Figure 7. Inbound data from days 270 to 180 pre-perihelion. Top panel: water production rate, same data as shown in Fig. 6 together with several spacecraft and empirical model parameters. Second panel: the empirical correction factor, *f*. Third panel: spacecraft latitude in comet-fixed coordinates (blue) and spacecraft phase angle. Fourth panel: spacecraft latitude (blue) and longitude (red) in Sun-fixed coordinates.

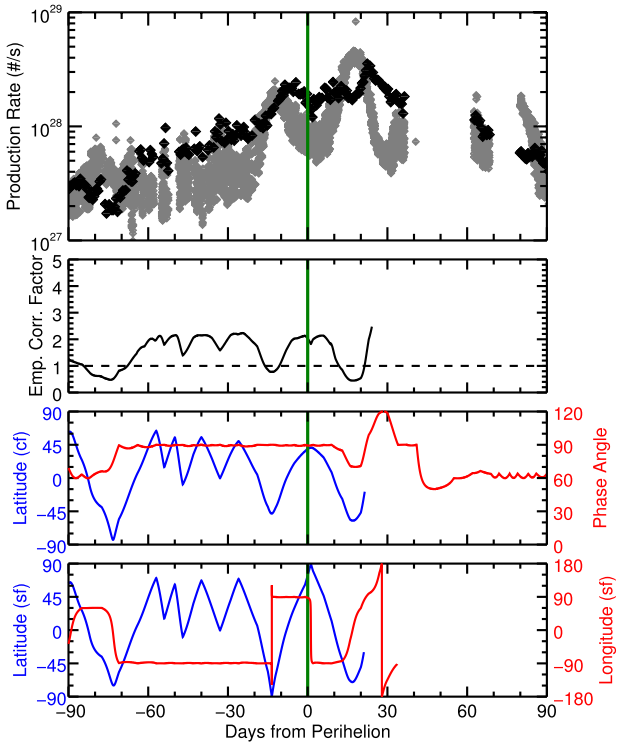

Figure 8. Perihelion data. Same quantities as Fig. 7.

the water production systematically underestimates the production rate. Also shown is the correlation between the spacecraft motion, the observed density and the empirical correction factor. When the spacecraft is at southern latitudes, the water density is low, therefore the correction factor must be high. The opposite is true at northern latitudes where the measured density is high, so the correction factor is low. During the pre-equinox period covered by Fig. 7, the empirical correction factor very effectively compensates for the spacecraft motion through the non-uniform water coma.

Fig. 8 is shown to contrast the very effective clear correction the empirical model makes before the inbound equinox with the potentially less effective correction made during perihelion. During the perihelion period, the water production has shifted to the Southern hemisphere. The empirical correction captures this shift and is clearly now phased so that the correction factor is high at northern latitudes (opposite from before equinox). However, within ±30 d of perihelion, the empirical model does not completely smooth out variations in the ROSINA data that appear to correlate with spacecraft motion. The apparent peaks in the detrended ROSINA data at ∼8 d pre-perihelion and ∼10 and ∼22 d post-perihelion are less certain and may indicate that there was time variability of the water production not associated with spacecraft motion, and that the empirical model may not be perfectly suited to modelling and correcting this period, or both.

3.2 VIRTIS-H and VIRTIS-M

Rosetta's VIRTIS-H instrument made initial measurements of the water coma by observing the vibrational band of H_2O at 2.67 μm from 2014 November 24 up to 2015 January 24, corresponding to a heliocentric distance ranging from 2.9 to 2.5 au (Bockelée-Morvan et al. 2015). Before that time, only limited detections of H_2O were obtained. These line-of-sight (LOS) measurements were performed by pointing the instrument 0.5–1 km off the nucleus limb of the Sun facing hemisphere and acquiring data during a period of 6 s each. While VIRTIS-H has three pixels, the signal is usually averaged to one data point. For the observed wavelength interval of 2.60–2.73 μm, Debout, Bockelée-Morvan & Zakharov (2016) show that for the encountered production rates, the coma is optically thin for the observed H_2O band, in which case, the computation of column densities from the band intensities is straightforward.

In order to convert observed column densities to a total water production rate, a model of the coma must be employed. To correct for the viewing geometry, Fougere et al. (2016b) use the DSMC model results to compute LOS column densities for each VIRTIS-H observation. Using the modelled column densities, the authors computed the correction factor as the ratio of the column densities from the data and the simulation results, respectively. Applying their correction factor, Fougere et al. (2016b) use the column densities reported by Bockelée-Morvan et al. (2015) to obtain a total water production rate. Without further modelling, this method works only for observations where the observed water line is optically thin.

In addition to the VIRTIS-H data, two water production rates, 2.5×10^{26} at 2.21 au and 4.65×10^{26} at 1.76 au, both inbound, have been published by Fink et al. (2016) using the VIRTIS-M sensor. VIRTIS-M is the high-spatial resolution channel of the VIRTIS instrument designed for spectral mapping. VIRTIS-M has two measurement bands, 0.22–1 μm in the visible and 1–5 μm in the infrared. Fink et al. (2016) study water production by using water emission at 2.7 μm in multiple image cubes take by VIRTIS-M at the two heliocentric distances. Fink et al. (2016) are particularly

interested in the water distribution during these two time periods, but they also calculate the total water production.

3.3 MIRO

MIRO (Microwave Instrument for Rosetta Orbiter) is another remote sensing instrument on Rosetta ((Gulkis et al. 2007)). In 2014 June, Gulkis et al. (2015) reported the first detection of H_2O in the coma of 67P/CG. For our study, we include the water production rates reported by Lee et al. (2015) and Biver et al. (2015). The former are obtained for 2014 August 7–9 and 18 and 19 observing the 556.936 GHz line of $H_2^{16}O$. The latter estimate the total H_2O production rate from measurements of the peak outgassing rate per solid angle of the optically thin $H_2^{18}O$ coma for 2014 September by assuming a ratio of 500 for $H_2^{16}O$ / $H_2^{18}O$ (in line with $^{16}O/^{18}O$ isotopic ratio found by Altwegg et al. 2015). During these observations, much of the coma of 67P/CG was contained in the field of view of the single pixel of the instrument, resulting in no need to correct for the nonuniform distribution of the water coma. When the comet is closer to the Sun, the MIRO observations of the water in 67P/CG are more difficult to convert from observations of emission to a total water production as the instrument has to be raster-scanned across the nucleus while the nucleus itself rotates underneath the spacecraft.

3.4 RPC/ICA

The Rosetta Plasma Consortium (RPC) is comprised of several instruments designed to characterize the plasma and magnetic environment of 67P/CG. Although none of the RPC instruments is designed to directly measure the neutral water coma, the water production can be inferred from plasma measurements using the He^+ to He^{2+} ion flux ratio that is a proxy of the charge transfer from the solar wind alpha particles to neutral water molecules. Simon Wedlund et al. (2016) used data from the Ion Composition Analyzer (ICA) instrument to determine the flux ratios above in approximate 6-h intervals to average out some of the diurnal neutral atmosphere variations. They then applied a simple analytical model taking into account photoionization of H_2O molecules and solar wind charge transfer, together with the assumption of a spherically symmetric water coma with a constant neutral gas velocity of 700 m s^{-1}. They estimated the water production rate over a heliocentric distance range from 3.3 to 1.9 au inbound, with the production rate following a $r_h^{-7.1}$ trend with heliocentric distance (r_h) in astronomical units. The 700 m s^{-1} velocity used by Simon Wedlund et al. (2016) is a constant and lies at the upper end of the velocity predicted by the empirical model (600–700 m s^{-1}) at these heliocentric distances, and therefore the productions rates calculated by Simon Wedlund et al. (2016) could may vary up to 15 per cent.

3.5 Ground-based observations

Snodgrass et al. (2016a,b) published results of an extended ground-based observation campaign covering the period from 4.4 au inbound to 2 au outbound after perihelion. There is a gap in the data on the inbound leg between 2.9 and 1.3 au due to low solar elongation and therefore bad viewing conditions. The perihelion passage also occurred at low solar elongation, but observations were possible from the Earth in very short windows during each morning for a given telescope. The observation schedule was best suited to robotic telescopes where a service/queue scheduled mode was possible.

Using telescopes listed in Snodgrass et al. (2016a), ground-based measurements show that 67P/CG was already active at heliocentric distances greater than 4 au and that its activity, throughout the perihelion passage, was very similar to previous apparitions. The published ground-based observations are not of the water coma, but comprise observations of the reflectance of sunlight off the dust coma. In contrast to the majority of measurements made by remote sensing instruments on Rosetta, the ground-based observations have the advantage of fitting the entire coma into a single measurement. For this reason, although the Rosetta measurements are of water density and the ground-based measurements are of dust reflectance, it is worth comparing the two heliocentric profiles. Snodgrass et al. (2016a) published the dust *R*-band magnitude corrected for viewing geometry. For the work presented here, we have converted the published magnitudes to brightness and then multiplied by an arbitrary scaling factor in order to compare the trend in production as a function of heliocentric distance.

4 DISCUSSION

Fig. 9 shows the water production of 67P/CG as a function of heliocentric distance as observed by Rosetta, together with the scaled ground-based dust measurements. The figure includes the detrended ROSINA data as well as the previously published VIRTIS-H, VIRTIS-M, MIRO, RPC/ICA and ground-based data. Although water production rates in the published literature exist for only a limited range of inbound heliocentric distances, the comparison of the different data sets is quite good. The MIRO data set, although limited, is important because it provides the only Rosetta measurements beyond 3.6 au. The ICA data, although one step further processed than the other Rosetta data, show very good agreement with both the ROSINA data as well as the VIRTIS-H data. The VIRTIS-H data have a trend that is consistent with the ROSINA data, with a scatter that is similar to the non-detrended and non-averaged ROSINA data (shown in Fig. 6). There does appear to be a systematic offset of the VIRTIS-H data below the ROSINA data of about a factor of 2. One possibility for the difference between the VIRTIS-H and ROSINA production rates may be the difference in acquisition techniques – during this period, ROSINA measures *in situ* between 20 and 30 km from the nucleus, while VIRTIS-H measures water emission along LOS that pass much closer to the nucleus. Closer to the nucleus, the gas activity may still be more confined than it is at larger cometocentric distances where ROSINA measures. A second possibility for the difference in the two data sets could be an extended source of water. Such a source would yield higher water production rates further from the comet and would therefore be consistent with ROSINA measuring a higher production rate than VIRTIS. However, the difference in radial distance of the two measurements (20–30 km) is not large enough to realistically account for the apparent factor of 2 difference in the two data sets.

In Fig. 9, the comparison between the ROSINA water production rate measurements and the scaled, ground-based dust measurements is extremely good given that we use only a single scaling factor over the entire range of the dust measurements spanning 4.4 au inbound to 2.0 au outbound. To first order, the dust brightness is a measurement of the available reflecting surface area in the dust coma. The high correlation between the dust brightness and the water production rate then indicates that the ratio of dust surface area to water production is nearly constant over the entire perihelion passage. The simplest way to explain such a strong correlation would be for the dust to gas ratio and the dust size distribution

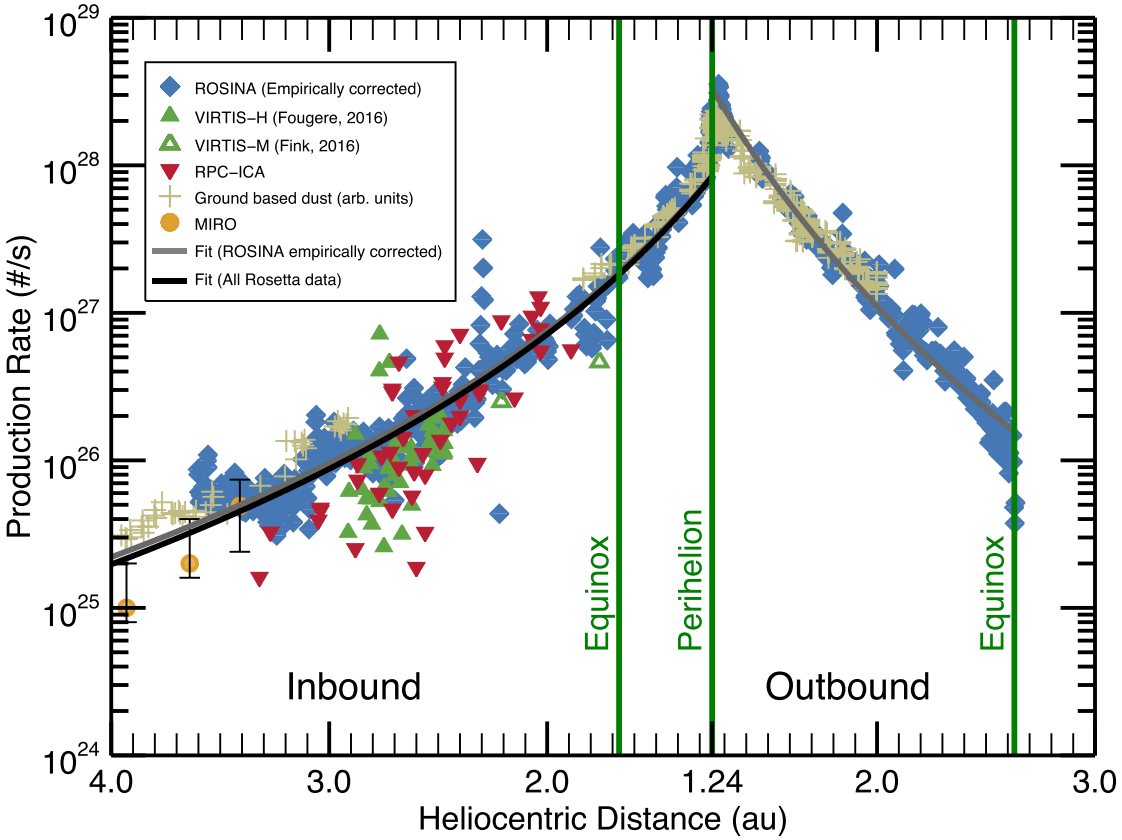

Figure 9. Water production rate as a function of heliocentric distance as determined by various Rosetta instruments and ground-based telescopes: ROSINA (corrected, blue diamonds), VIRTIS (green triangles) (Bockelée-Morvan et al. 2015; Fink et al. 2016; Fougere et al. 2016b), RPC/ICA (red triangles) (Simon Wedlund et al. 2016), MIRO (yellow circles) (Biver et al. 2015; Lee et al. 2015), ground-based (tan crosses) (Snodgrass et al. 2016a). Note that the ground-based data are not water productions, but are dust brightnesses and have been scaled using an arbitrary scaling factor for the sake of comparison. The grey line indicates a fit to the ROSINA data, while the black curve indicates a fit to all inbound Rosetta data. Fit parameters are given in Table 2.

to remain over the same period. If the dust to gas ratio and dust size distribution are not constant, then they would need to evolve consistently so that a change in the dust to gas ratio would be balanced by a change in the size distribution in such a way that the sun light reflecting surface area of the dust coma remained proportional to the water production. It is hard to imagine that this would be the case.

We will discuss features of the 67P/CG water production in the order encountered by the spacecraft, starting with observations made during the inbound Rosetta period outwards of 3.0 au. During this period, we rely on ROSINA data and the limited published MIRO results. Fig. 6 shows that during this period, the uncorrected ROSINA data decrease as the heliocentric distance decreases. After applying the empirical correction, the water production is more constant. During this period, Rosetta was approaching the comet from the day side where the water production is a maximum and where using a spherically symmetric coma model leads to an overestimation of the production. Although the empirical model corrects for this, the corrected ROSINA water production does not show an increase with decreasing heliocentric distance as expected, instead showing a relative plateau in water production during this period. It is interesting to note that the scaled ground-based data, although strictly a measure of dust, not water, show a similar plateau during this period. The published MIRO data are sparse during this period, but the three points are consistent with the weak growth in dust measurements inbound beyond 3.6 au and with the ROSINA water production value at 3.5 au. The MIRO measurements and the ground-based dust measurements beyond 3.6 au may indicate that 67P/CG experienced a rapid increase of water production just before Rosetta rendezvous at 3.6 au.

Of considerable interest is the behaviour of the water production during 67P/CG's passage through the inbound equinox. Observations by all Rosetta instruments show that before equinox, the water production peak was at northern latitudes, while after equinox, the water production shifted to southern latitudes. Figs 2 and 10 highlight the contribution of the DSMC model of Fougere et al. (2016b) for our understanding of this transition. Fig. 2 shows the water distribution at 32 km from the nucleus, while Fig. 10 shows the water production on the nucleus that depends on both the spherical harmonic activity map generated by Fougere et al. (2016b) (see fig. 5 in their paper) as well as the solar illumination. The panels of Figs 2 and 10 correspond so they can be compared to understand the relationship between the density distribution and the production. The figures show that before equinox (3.5 au, and other runs at 2.7 and 2.2 au, not shown), there is a clear, single water production peak in the Northern hemisphere irrespective of the rotation phase. At 1.7 au, just before equinox at 1.67 au, the water production peaks mostly in the north, but there are rotation phases where the water production peaks only in the south and cases where there is a clear peak in both the north and the south. The rotational average for the 1.7 au case is clearly still in the north. Considering the 1.5 au case, just after the equinox, we find results in some ways similar to

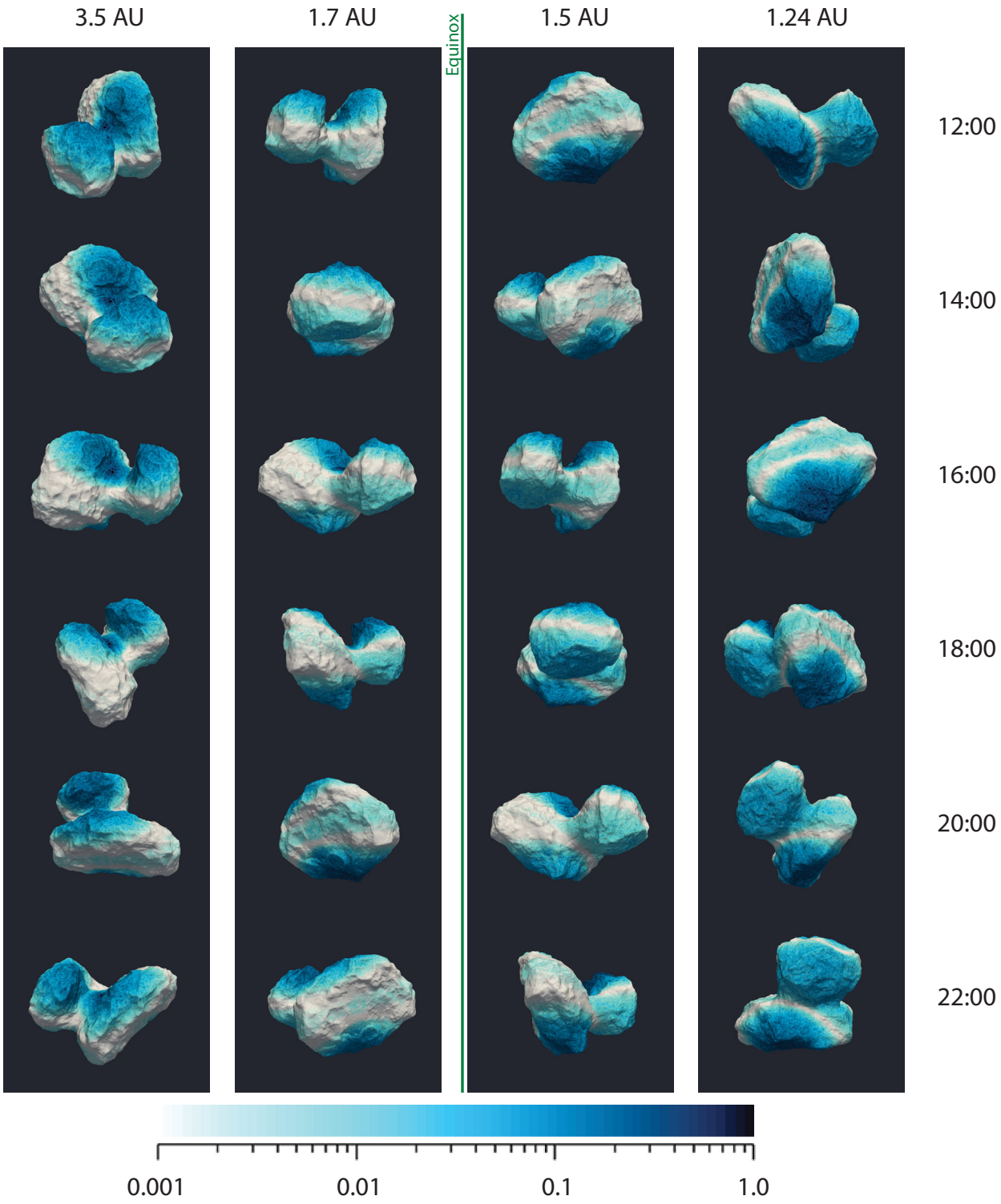

Figure 10. Water production rate from the surface of 67P/CG for the DSMC model runs. Each panel of the figure corresponds to the same panel in Fig. 2. However, here we are looking at the comet body from the sun and plotting the scaled water production rate. Columns represent four different interesting heliocentric distances while rows represent the different rotation phases. This figure can be compared panel by panel to Fig. 2 to better understand the water production as a function of heliocentric distance and rotation phase.

the 1.7 au case – there are cases that peak in the north, the south and both. However, for the 1.5 au case, most of the rotation phases and the rotationally averaged case show a clear, major peak in the south. The reason for this behaviour is clear in Fig. 10. The DSMC model of Fougere et al. (2016b) uses an spherical harmonic activity map for the production of water. The map has two locations that have large water production peaks: the neck region in the north and a region on the large lobe in the south. When these regions are

illuminated, they contribute a significant fraction of the total water production. When these regions are not illuminated, there is a more distributed water production. The DSMC model results therefore show that there is a dramatic shift of the average water production peak from the north to the south across the equinox and that the maximum production is rarely at the sub-solar point. The dramatic shift results in the preferential illumination of the northern or the southern activity map enhancements. The peak water production occurs before equinox at a sf-latitude of ∼55° above the Sun-comet line, while after equinox, the water peak was at an sf-latitude of ∼−50°. Although the transition of the average production across equinox is dramatically discontinuous, shifting one major peak from the north to the south, it is clear that during the transition, there is a complex water production distribution with production peaks in both the north and the south depending on the rotation phase.

Given the dramatic shift in the location of the water production peak, it would be reasonable, for there, to be a strong indication of the equinox crossing in the water production curve. Fig. 6 does show a modest, short-lived increase in the slope of the water production curve at equinox that results in an increase of production of about a factor of 2. However, the increase is not as evident when plotted as a function of heliocentric distance in Fig. 9, and in both figures, the increase does seem similar to other variations in the production rate at other times. Furthermore, as outlined above, the uncertainties associated with the empirical correction are the highest at equinox, so it is hard to separate any true increase from uncertainty potentially associated with the empirical correction. Although the evidence in Figs 6 and 9 are not definitive, Fougere et al. (2016a) indicate that their processing of ROSINA data, using a different but similar correction of the production rate based on the same DSMC model runs, show a clear production rate increase at equinox in each of the four major species H_2O, CO_2, CO and O_2. Based on the work of Fougere et al. (2016a) and Figs 6 and 9, it appears that there may have been a small increase in the production rate of water at equinox. However, as Fig. 6 shows, the production rate increase is not nearly as dramatic as the peak location shift.

After equinox, the next most interesting period of evolution of water production is the perihelion passage of 67P/CG. Fig. 8 shows the ROSINA data within ±90 d of the perihelion passage. As noted above, after application of the empirical model to detrend the spacecraft motion, three apparent peaks remain at ∼8 d pre-perihelion and ∼10 and ∼22 d post-perihelion. These three peaks are potentially important because, if not spacecraft motion-related, they represent a significant time variation of the water production. We note that non-corrected ROSINA data (proportional to the number density) are very well anticorrelated with the spacecraft motion (see Fig. 8, second and fourth panel) seeming to imply that they are spacecraft motion-related. However, the empirical model does not completely remove these peaks and, in fact, shifts them both in time and creates three smaller peaks, implying that either the empirical model is missing details related to the perihelion passage or that the peaks represent significant time variability of either production rate, distribution or gas velocity. Although there is some uncertainty of the ROSINA peaks due to the potential inadequacies of the empirical model correction, there is corroborating evidence from VIRTIS that water production near perihelion showed significant time variability. Bockelée-Morvan et al. (2016) indicated that VIRTIS measured an abrupt increase in water production 6 to 7 d after perihelion. This time would correspond to the smallest of the three peaks in the empirically corrected ROSINA data. Further study will be required to determine with high certainty the validity of these peaks. Despite these uncertainties, it is very clear that the water production peaks after perihelion. Considering the uncorrected production rate peak, the empirically corrected production rate peak and taking into account the uncertainties associated with the perhaps imperfect spacecraft motion subtraction, we find a peak water production of $(3.5 \pm 0.5) \times 10^{28}$ molecules s^{-1} observed 18–22 d after perihelion.

Table 3. Estimated perihelion passage mass-loss.

Component	Dust/gas	Mass-loss ($\times 10^9$ kg)	per cent loss (per cent)	Depth loss (m)
H_2O gas	–	6.4	0.06	0.3
All gas[1]	–	7.9	0.08	0.4
All gas[2]	–	9.2	0.09	0.4
Gas + dust	4	39–46	0.4	1.8–2.1
Gas + dust	6	55–65	0.6	2.3–3.0
Gas + dust	8	71–83	0.8	3.3–3.8

[1]Perihelion values: 91 per cent H_2O, 5 per cent CO_2, 2 per cent CO, 2 per cent O_2

[2]Average values: 83 per cent H_2O, 10 per cent CO_2, 5 per cent CO, 2 per cent O_2

The high-time and spatial resolution Rosetta data allow us to address the evolution of the water production rate over the entire range of Rosetta measurements spanning heliocentric distances of 4.0 au (inbound), through perihelion at 1.24 au, and outbound to just before the outbound equinox at 2.6 au. Fig. 9 shows a fit to the ROSINA data as well as a fit to the combined Rosetta data set (ROSINA, VIRTIS, RPC/ICA and MIRO). ROSINA data are fit for both the inbound and outbound passage while the combined Rosetta data set is fit for only the inbound passage. In each case, we fit the data to

$$Q = c_1 r_h^{c_2}, \tag{10}$$

where c_1 and c_2 are the fit coefficients given in Table 2, while r_h is the heliocentric distance in astronomical units. The table shows that the ROSINA fit parameters are very well constrained, a result of the low scatter in the data. When fitting all the inbound Rosetta data, the parameters are nearly identical to the ROSINA only fits, but the 1σ range of the values is much larger due to the significant scatter in the other data sets. Inbound fits to the Rosetta data show a very different slope than the outbound slope of the ROSINA data, with the outbound slope being significantly steeper than the inbound slope. The heliocentric dependence of the water production should provide an important constraint on the near-surface model of 67P/CG and how water is liberated from the surface. Keller et al. (2015) consider a two-layer model (a porous dusty layer above an icy layer) and are able to match water production from previous perihelion passages. However, that data extended to only ∼1.75 au. The model makes predictions out to 5 au, but each of the cases considered produced significantly more water far from the Sun than is observed by Rosetta. That work does indicate that thicker dust layers can reduce the water production, perhaps indicating that the steep water production curve is a result of insulation of the ice by porous dust.

Finally, we have estimated the mass lost during the perihelion passage observed by Rosetta using the water production rate curve calculated here combined with the spacecraft trajectory (see Table 3). Using the water production rate curve corresponding to all the Rosetta data in Table 2 and integrating over the period spanning 3.6 au inbound to 3.0 au outbound, we obtain a mass-loss of water of 6.4×10^9 kg. Integrating to larger heliocentric distances does not change the number significantly as most mass is lost near

perihelion. In order to estimate the total mass lost during the current orbit of 67P/CG, we include the major gas volatiles using relative abundances of H_2O, CO_2, CO and O_2 as measured by ROSINA (Hässig et al. 2015; Fougere et al. 2016a). The table includes a low estimate using perihelion abundances and a high estimate using abundances that are a rough average over the ROSINA data (see Fougere et al. 2016a, Fig. 12). Fougere et al. (2016a) show that the VIRTIS CO_2 column densities are consistent with the DSMC model of the ROSINA CO_2 densities at perihelion. However, we noted above that ROSINA H_2O measurements are consistently higher than VIRTIS. This results in VIRTIS measuring a higher relative abundance of CO2 at perihelion (Bockelée-Morvan et al. 2016) than the ROSINA numbers given in Table 3. Including these heavier species in the calculation increases the number density by 10–20 per cent, while, at the same time, increasing the mass-loss by nearly 25–45 per cent due to the larger masses of these molecules. Finally, although the dust to gas ratio is not a quantity measured by ROSINA, we estimate the total mass lost during this perihelion due to both gas and dust. Table 3 shows the estimated mass-loss for three different dust to gas ratios that cover the range of reported 67P/CG values (Fulle et al. 2015; Rotundi et al. 2015). The approximate mass-loss for this perihelion passage is 4–8 $\times$ 10^{10} kg. Using the same degraded version of the SHAP5 model of 67P/CG's shape (Preusker et al. 2015) as in Fougere et al. (2016b), we calculate a surface area of 46.6 km^2 and from that, we calculate the depth loss during this perihelion passage assuming uniform loss across the surface. We find a depth change of about 2–4 m.

5 CONCLUSIONS

We presented observations and analysis of the water production rate measured by the various Rosetta instruments as well as through Earth-based telescopes. We present details of the water production evolution over the period spanning 4.0 au inbound to 2.7 au outbound corresponding to the escort phase of the Rosetta mission and the perihelion passage of comet 67P/Churyumov–Gerasimenko. Water production rates are calculated from the ROSINA DFMS and COPS measurements of the number density using an empirical model of the non-uniform gas coma to correct for the spacecraft motion as a function of heliocentric distance, radial distance from the comet, Sun-fixed longitude and latitude and then averaged over a cometary rotation period. The empirical model is applicable to 67P/CG water production starting at 3.5 au inbound and continuing through the outbound equinox. We also present, for comparison, previously published water production rate data from the MIRO, VIRTIS-H and RPC/ICA instruments. In general, the agreement between the instruments is very good, although the VIRTIS-H productions are lower than the ROSINA productions rates by approximately a factor of 2. There are potentially several explanations for this difference, including differences in observing geometry and the possible release of additional H_2O due to an extended source.

We have shown that the dust coma brightness, as measured by ground-based telescopes, and the water production measured *in situ* by the ROSINA instrument are highly correlated. Such a high correlation may indicate the possibility that the dust to gas ratio and the dust size distributions are constant during the entire perihelion passage of 67P/CG.

We have shown that the water production should be discussed in several different phases in order to fully understand both the distribution of water production on the surface and also the trend with heliocentric distance. Early in the mission (beyond 3.5 au), the ROSINA water production does not show the expected increase with decreasing heliocentric distance, similar to the dust brightness measurements. A second important phase is the transition through the inbound equinox, where the water production makes a dramatic transition from maximum production in the north to maximum production in the south. We showed that the Fougere et al. (2016b) model shows a rapid transition of the rotationally averaged production from a peak at $\sim$55°N to $\sim$50°S, while, at the same time, showing that at certain rotation phases, there are peaks in both the north and the south around the same time. Another significant phase of the water production is the time period about perihelion, where there may be evidence of two or three time-dependent increases in the water production, although more modelling is required to verify their identification. The peak of water production occurs 18–22 d after perihelion with peak production of (3.5 $\pm$ 0.5) $\times$ 10^{28} molecules s^{-1}.

Finally, we analysed the heliocentric dependence of the water production with the result that a power law with exponents of -5.3 inbound and -7.1 outbound fits all the available Rosetta data well, showing a much steeper drop in the water production after perihelion than the rise before perihelion. A simple calculation of the amount of mass lost through the water production and a simple estimate of the dust/gas ratio showed that, roughly, an average of 2–4 m of surface depth could have been lost during this perihelion passage if the loss were spread uniformly over the surface.

ACKNOWLEDGEMENTS

This work was supported by contracts #1266313 and #1266314 from the Jet Propulsion Laboratory under the US Rosetta Project and NASA grant NNX14AG84G from the Planetary Atmospheres Program. Work at University of Bern was funded by the State of Bern, the Swiss National Science Foundation, and by the European Space Agency PRODEX Program. Work at Southwest Research institute was supported by subcontract #1496541 from the Jet Propulsion Laboratory. Work at The Royal Belgian Institute for Space Aeronomy was supported by the Belgian Science Policy Office via PRODEX/ROSINA PEA C4000107705 and an Additional Researchers Grant (Ministerial Decree of 2014-12-19), as well as by the Fonds de la Recherche Scientifique grant PDR T.1073.14 'Comparative study of atmospheric erosion'. Work at University of Oslo was supported by the Research Council of Norway grant No. 240000. ROSINA would not give such outstanding results without the work of the many engineers, technicians, and scientists involved in the mission, in the Rosetta spacecraft, and in the ROSINA instrument team over the last 20 yr whose contributions are gratefully acknowledged. The authors would like to thank the space agencies of Italy (ASI), France (CNES), German (DLR) and US (NASA) for supporting this research. The authors wish to thank the Rosetta Science Ground Segment and the Rosetta Mission Operations Centre for their continuous support. Rosetta is an ESA mission with contributions from its member states and NASA.

REFERENCES

Altwegg K. et al., 2015, Science, 347, 1261952
Balsiger H. et al., 2007, Space Sci. Rev., 128, 745
Bensch F., Bergin E. A., Bockelée-Morvan D., Melnick G. J., Biver N., 2004, ApJ, 609, 1164
Bertaux J.-L., Combi M. R., Quémerais E., Schmidt W., 2014, Planet. Space Sci., 91, 14
Bieler A. et al., 2015, A&A, 583, A7

Biver N. et al., 2002, Earth Moon Planets, 90, 5
Biver N. et al., 2015, A&A, 583, A3
Bockelée-Morvan D., Crovisier J., Mumma M. J., Weaver H. A., 2004, in Festou M. C., Keller H. U., Weaver H. A, eds, Comets II. Univ. Arizona Press, Tucson, AZ, p. 391
Bockelée-Morvan D. et al., 2015, A&A, 583, A6
Bockelée-Morvan D. et al., 2016, MNRAS, 462, S170
Combi M. R., Mäkinen J. T. T., Bertaux J.-L., Quemérais E., 2005, Icarus, 177, 228
Debout V., Bockelée-Morvan D., Zakharov V., 2016, Icarus, 265, 110
Fink U. et al., 2016, Icarus, 277, 78
Fougere N. et al., 2016a, MNRAS, 462, S156
Fougere N. et al., 2016b, A&A, 588, A134
Fulle M. et al., 2015, A&A, 583, A14
Gehrz R. D., Hanner M. S., Homich A. A., Tokunaga A. T., 2005, AJ, 130, 2383
Guilbert-Lepoutre A., Schulz R., Rożek A., Lowry S. C., Tozzi G. P., Stüwe J. A., 2014, A&A, 567, L2
Gulkis S. et al., 2007, Space Sci. Rev., 128, 561
Gulkis S. et al., 2015, Science, 347, aaa0709
Hartogh P. et al., 2010, A&A, 518, L150
Hartogh P. et al., 2011, Nature, 478, 218
Haser L., 1957, Liége Inst. Astrophys., Reprint No. 394
Hässig M. et al., 2015, Science, 347, aaa0276
Keller H. et al., 1986, Nature, 321, 320
Keller H. U. et al., 2015, A&A, 583, A34
Kührt E., 1999, Space Sci. Rev., 90, 75
Lara L. M., Lin Z.-Y., Rodrigo R., Ip W.-H., 2011, A&A, 525, A36
Lecacheux A. et al., 2003, A&A, 402, L55
Lee S. et al., 2015, A&A, 583, A5
Ootsubo T. et al., 2012, ApJ, 752, 15
Preusker F. et al., 2015, A&A, 583, A33
Rotundi A. et al., 2015, Sci, 347, aaa3905
Sagdeev R. Z. et al., 1986, Nature, 321, 262
Schleicher D. G., 2006, Icarus, 181, 442
Schulz R., Stüwe J. A., Boehnhardt H., 2004, A&A, 422, L19
Simon Wedlund C. et al., 2016, A&A, 587, A154
Snodgrass C. et al., 2016a, MNRAS, 462, S138–S145
Snodgrass C. et al., 2016b, A&A, 588, A80
Tenishev V., Combi M., Davidsson B., 2008, ApJ, 685, 659
Tenishev V., Combi M. R., Rubin M., 2011, ApJ, 732, 104
Tubiana C., Böhnhardt H., Agarwal J., Drahus M., Barrera L., Ortiz J. L., 2011, A&A, 527, A113
Weaver H. A., Feldman P. D., Festou M., A'Hearn M. F., Keller H. U., 1981, Icarus, 47, 449
Weiler M., Rauer H., Helbert J., 2004, A&A, 414, 749
Whipple F. L., 1950, ApJ, 111, 375

SUPPORTING INFORMATION

Supplementary data are available at *MNRAS* online.

2016_CG_ProductionRate_v4_diff.pdf

Please note: Oxford University Press is not responsible for the content or functionality of any supporting materials supplied by the authors. Any queries (other than missing material) should be directed to the corresponding author for the paper.

This paper has been typeset from a TEX/LATEX file prepared by the author.